Nanoscale

PAPER

View Article Online
View Journal

Cite this: DOI: 10.1039/d5nr04109k

Carbon fibers with infiltrated TiO_2 nanocrystalline layers: photocatalytic performance

Pavan Kumar Chennam, [a] Martina Rihova,[a] Susan Azpeitia, [b] Marcela Sepúlveda,[a,c] Martin Kachlík, [a] Miloslav Pouzar,[c] Veronika Čičmancová,[c] Karel Maca,[a] Mato Knez [b,d] and Jan M. Macak *[a,c]

Received 28th September 2025,
Accepted 30th November 2025

DOI: 10.1039/d5nr04109k

rsc.li/nanoscale

This study examines the synergy of carbon fibers (CFs) and an infiltrated TiO_2 nanocrystalline layer for photocatalytic degradation of methylene blue (MB). The CFs@TiO_2 nanocomposite was developed using Vapour Phase Infiltration (VPI) of TiO_2 into polyacrylonitrile fibers with 5–160 infiltration cycles and subsequently carbonized at 900 °C. This integrated production method enables precise integration of TiO_2 and consistent coating over the fiber surface. SEM confirms the TiO_2 layer thickening from 15.7 ± 2.4 nm to 34.7 ± 3.4 nm as the cycles increase from 40 to 160, while EDX and EDXRF indicate a similar rise in TiO_2 content. XRD and Raman spectroscopy confirm the production of anatase TiO_2 for VPI 40 c and higher, attributed to size-induced crystallization. UV–Vis DRS demonstrates that the optical bandgap varies with the cycle number in accordance with the development of the TiO_2 layer. The outcomes of photocatalytic experiments under UV illumination indicate that the maximum degradation rate is achieved with the thickest coating. The CFs@TiO_2 demonstrate exceptional cycle stability. This study emphasizes the potential of VPI-derived CFs@TiO_2 as durable and effective photocatalysts.

Introduction

Water is the source of life for all animals, plants, insects, and humans, and it is the most important element of the ecosystem. However, industrial discharge, agricultural runoff, and inappropriate waste disposal release hazardous substances into the environment, thereby contaminating natural water resources.[1] According to studies, industrial wastewater releases approximately 280 000 tons of dyes each year.[2] Without proper treatment, these will have a significant environmental impact, including spoilage of drinking water and crops upon watering. In particular, methylene blue (MB) is a widely used dye in several industries, including clothing,[3] textiles,[4] ink,[5] pharmaceuticals,[6] and paper.[7] The release of MB-spoiled wastewater into the environment adds significantly to eutrophication and poses serious health hazards such as cancer, eye burns, mutations, skin irritations, and allergic dermatitis.[8] As a result, MB – as well as any other synthetic dye – must be efficiently removed from the water before its discharge into the environment.

A variety of methods for the removal of MB and other dyes from wastewater have been investigated, including ozonation,[9] adsorption,[10] biodegradation,[11] chlorination,[12] electrochemical treatment,[13] membrane filtration,[14] photocatalysis,[15–17] chemical coagulation,[18] oxidation,[19] activated carbon adsorption,[20] and reverse osmosis.[21] These techniques can effectively eliminate dyes from industrial wastewater. Among them, photocatalysis is a simple and effective process for treating water contaminants without secondary pollution. It utilizes renewable solar energy to convert organic compounds into harmless and non-toxic small molecules.[22–26]

Semiconductor photocatalysts (SPs) are preferred materials for photocatalytic treatments of dyed wastewater for being (i) cost-effective; (ii) non-toxic; (iii) tunable with respect to their properties through size-alteration, doping, or sensitization; (iv) able to facilitate a multielectron transfer process; and (v) applicable for extensive periods without a significant decrease in photocatalytic activity.[27] Titanium dioxide (TiO_2)[28] was chosen as a photoactive catalyst due to its strong photoactivity, chemical stability, non-toxicity, good resistance to photocorrosion, and low cost.[28] It retains activity upon long irradiation as compared to other metal oxides, such as zinc oxide (ZnO),[29] tungstate trioxide (WO_3),[30] and cerium dioxide (CeO_2).[31] Among the several polymorphs of TiO_2,[32] the anatase phase is the most suitable for photocatalytic applications due to its high surface area, efficient charge transport, and strongly oxidizing ability for radical generation.[33] However, the applicability of

[a]Central European Institute of Technology, Brno University of Technology, Purkynova 123, 61200 Brno, Czech Republic. E-mail: jan.macak@upce.cz
[b]CIC nanoGUNE BRTA, Tolosa Hiribidea 76, E-20018 Donostia/San Sebastian, Spain
[c]Center of Materials and Nanotechnologies, Faculty of Chemical Technology, University of Pardubice, Nam. Cs. Legii 565, 53002 Pardubice, Czech Republic
[d]Ikerbasque, Basque Foundation for Science, Plaza Euskadi 3, E-48009 Bilbao, Spain

TiO_2 photocatalysts is significantly limited due to low quantum efficiency and ineffective utilization of visible light. These limitations result from the high recombination rate of photo-generated electron–hole pairs and the wide optical band gap, respectively.[34,35] A variety of methods have been developed to extend the lifetime of photo-generated electron–hole pairs and narrow the band gap, including coupling with further narrow band gap semiconductor materials,[36,37] modification with metal and nonmetal elements,[38–40] surface sensitization by organic dye molecules,[41,42] and hydrogen plasma treatment,[43–45] among others. Among these methods, nonmetal doping is most promising to overcome the problem of ineffective use of visible light and high carrier recombination rate.[46–48]

The graphitic nature of C provides multiple benefits because of its exceptional features, which include large surface area, porosity, adsorption capacity, and conductivity.[49] The material exhibits metal-like electron-storage properties, which enable it to accept photo-generated electrons (e^-_{CB} in conduction bands) and holes (h^+_{VB} in valence bands).[49] Additionally, when combined with a wide band gap semiconductor (*e.g.*, TiO_2), graphitic C can decrease the bandgap energy of it, which enhances the TiO_2 photocatalytic activity and extends its absorption range.[49,50]

A composite of C and TiO_2 generates synergies that can be advantageously leveraged. TiO_2 provides chemical stability and effective photocatalytic activity in the UV, while C, preferably in the form of fibers (CFs), provides a conductive scaffold that facilitates electron transfer and charge carrier separation to reduce electron–hole recombination.[51] Also, carbon can provide porosity, allowing a high surface area for the degradation of pollutants. The optical properties of carbon enable the photocatalyst to absorb visible light in the spectral range, which may also enhance the reactivity of TiO_2. All aforementioned attributes will contribute to a stable, robust, and potentially broadband responding photocatalyst, which may outperform TiO_2 itself.

There are many methods to deposit TiO_2 on carbonaceous supports, including sol–gel processing,[52,53] dip coating,[54,55] sputtering,[56] Chemical Vapor Deposition (CVD),[57] and electrochemical deposition.[58] Table S1 summarizing carbon-based TiO_2 photocatalysts, synthesized by various routes, is provided in the SI. Although these techniques are commonly used, they experience limitations such as poor coating uniformity and weak adhesion between the coated material and the support. These challenges can be addressed through Atomic Layer Deposition (ALD)[59–62] which is known for excellent adhesion of the coatings to the underlying substrates due to chemical bonding, exceptional conformality, and large-area homogeneity, together with precise control over atomic-level thickness and composition. ALD is a unique modification of the CVD process that involves alternating supply of two (or more) vaporized precursors to the substrate, one at a time. The coating formation occurs cyclically, involving a sequence of surface reactions between the adsorbing precursor and the species formed on the surface following the prior precursor pulse. Depending on the processing conditions used, the deposited coatings might be amorphous, single crystalline, or polycrystalline. ALD offers distinct benefits over other thin film deposition techniques: ALD-grown coatings exhibit excellent uniformity and conformality, are pinhole-free, contain minimal contaminants, can coat porous and high aspect ratio nanomaterials, and can form strong chemical bonds with the substrate, thus assuring very strong adhesion.[63–65] ALD may be performed at lower temperatures (<100 °C) than CVD, minimizing thermal damage to delicate substrates such as bioorganic species, organic media, and polymers.[66,67] In particular, the literature has documented two different core approaches for applying ALD principles to polymeric fibers. The first approach, pioneered by Parsons's group,[68] grows ALD coating on the surface of polymer fibers that act as sacrificial templates to produce microtubes after thermal degradation of the polymeric fibers. This approach was used, *e.g.*, to create TiO_2 microtubes, based on the ALD of TiO_2 on electrospun[69] and centrifugal spun poly (vinylpyrrolidone) fibers[62] and their subsequent burnout. The second approach is called Vapour Phase Infiltration (VPI) or Sequential Infiltration Synthesis (SIS), and it was developed by Knez's group.[70,71] VPI introduces gaseous precursors into the subsurface of organic materials, causing chemical interactions with the chemical functionalities of the substrate and growing inorganic materials inside the bulk. Thus, unlike ALD, which generates a surface coating, VPI additionally modifies the bulk of the substrate, resulting in a novel organic–inorganic hybrid material[72] with increased chemical stability.[73] During the VPI process, a solid polymer or small molecule substrate is exposed to a vaporized metal-containing precursor. Depending on the precursor and substrate chemistry, as well as the VPI processing settings, the precursor will sorb, diffuse, and get entrapped. Entrapment happens by chemical contact with the substrate or reaction with a co-reactant that is subsequently provided, resulting in a nonvolatile substance, often a metal oxide cluster of only a few atoms in size.

In terms of fiber synthesis itself, in addition to the well-known process of electrospinning.[74,75] Another flexible and largely scalable bottom-up approach used for making one-dimensional fibers is centrifugal spinning. The advantages of centrifugal spinning over electrospinning have been extensively reported and evaluated in the literature,[76,77] including their higher production rates, less hazards (no electrostatic charge to ignite the organic solutions), improved reproducibility, and dimensional control.[76] This technique has demonstrated efficiency in producing fibers with diameters ranging from sub-micron to micrometer scales in a straightforward and cost-effective manner. Recent years have evidenced effective production of fibers *via* centrifugal spinning, employing polymers such as polyvinyl alcohol,[78] poly(vinylidene fluoride),[79] polycaprolactone,[80] biopolymers,[81] and inorganic fibers, including WO_3,[82] ZrO_2,[83] SiO_2,[84] Co_3O_4,[85] Fe_2O_3,[86] SnO_2[87] and Al_2O_3.[88]

The pioneering work of E. Fitzer *et al.*[89] showed that CFs can be obtained from PAN fibers through carbonization. This work deepened our understanding of the microstructure and how properties can be modified during the PAN-to-C transformation. In our recent study[90] We demonstrated for the first

time that CFs can also be synthesized from centrifugally spun PAN fibers.

This study reports a contemporary and scalable method for producing CFs infiltrated with TiO_2 (CFs@TiO_2). We combined for the first time centrifugal spinning, Vapour Phase Infiltration, and carbonization. Initially, PAN fibers were produced by centrifugal spinning to form a scaffold. Then TiO_2 was infiltrated into these polymer fibers in various doses by using various VPI cycles ranging from 5 to 160, eventually resulting in PAN@TiO_2. The resulting PAN@TiO_2 fibers were carbonized at 900 °C, forming conductive CFs with embedded TiO_2. The key benefit of this method is the ability to manage the TiO_2 incorporation, morphology, and loading *via* the number of performed VPI cycles. An extensive range of characterization techniques, including SEM, EDXRF, EDX, XRD, Raman spectroscopy, and UV–Vis diffuse reflectance spectroscopy, was utilized to characterize the morphological, chemical, structural, and optical properties of the CFs@TiO_2 composites. The photocatalytic activity was assessed through MB degradation under ultraviolet light (λ = 365 nm), considering reaction kinetics and reuse performance. This synthesis route provides an economical and scalable method to develop stable, reusable photocatalysts.

Experimental

Materials

DOLAN GmbH, Germany, provided polyacrylonitrile granulate (molecular weight 116 000 g mol^{-1}, N-PAN). Penta Chemicals (Czech Republic) supplied *N*,*N*-dimethylacetamide (DMAC, minimum 99.5 wt%), utilized as a solvent for PAN.

Centrifugal spinning of polyacrylonitrile (PAN) fibers

At room temperature, PAN was dissolved in DMAC using vigorous stirring. The solution had a concentration of 15 wt% and weighed 300 g. The PAN solution was centrifugally spun using Cyclone Pilot G1 (centrifugal spinning pilot equipment, Pardam Nano4Fibers Ltd, Czech Republic). The following processing conditions were employed for fiber production: a temperature of 35 ± 5 °C, a rotational speed of 10 000 rpm, and a relative humidity (RH) of 25 ± 5%. In the form of bulky 3D structures, the resultant fibers were collected and desiccated in the air.[84]

Vapour phase infiltration of TiO_2 into fibers (PAN@TiO_2)

The VPI process was performed in a custom-built fluidized bed reactor. To achieve the infiltration of TiO_2 into the PAN fibers, they were exposed to precursor vapors for a defined period of time -exposure time- to promote the diffusion of precursor into the near-surface region of the fibers rather than strictly limiting the reactions to the outer surface. PAN fibers, with a glass transition temperature (T_g) of 85–100 °C,[91] were processed at 80 °C. Using a temperature close to the T_g promotes greater mobility of polymer chain segments, allowing the precursors to penetrate deeper into the fiber subsurface. PAN fibers in 1.5 g doses were introduced into a stainless-steel column with an internal diameter of 25 mm and a height of 250 mm. During the process, a heating jacket was wrapped around the reactor to keep the bed temperature in control. Titanium Tetrachloride ($TiCl_4$) functioned as the precursor for TiO_2, with water (H_2O) acting as the source of oxygen. High-purity nitrogen, with a concentration of 99.9999%, was utilized as a carrier and purging gas at a flow rate of 150 standard cubic centimeters per minute (sccm). Under the specified deposition conditions, a single growth VPI cycle is defined by the following sequence: $TiCl_4$ pulse (2 seconds)—exposure (90 s)—N_2 purge (360 s)—H_2O pulse (1.5 s)—exposure (90 s)—and N_2 purge (360 s). Several VPI cycles were applied, specifically 5, 10, 20, 40, 80, and 160 cycles. The samples were labelled as 5c, 10c, 20c, 40c, 80c, and 160c, respectively.

Carbonization processes

The process for obtaining CFs has been elucidated in previous studies.[90] To ensure the stabilization of the PAN fibers, they were subjected to annealing in an XERION XRETORT 1200 furnace at 240 °C for 60 min, employing a rise rate of 1 °C min^{-1}. The stabilized fibers were carbonized in an argon atmosphere at 900 °C with a heating rate of 5 °C min^{-1}. After achieving the optimal temperature for carbonization, the furnace was allowed to cool naturally to room temperature.

Photodegradation tests

The photocatalytic activity of CFs and CFs@TiO_2 was assessed by the photocatalytic degradation of a methylene blue solution (MB; initial concentration = 1×10^{-5} M). CFs and CFs@TiO_2 are hydrophobic by nature; to increase their wettability (*i.e.*, to become more hydrophilic), 10 mg of the sample were immersed in the MB solution (V_{total} = 30 ml) and centrifuged at 11 000 rpm for 3 min. Subsequently, the samples were sonicated for 5 min at 100% power, 37 kHz using an FB11203, Fisherbrand in DI water. Before carrying out measurements, 10 mg of the sample was immersed in the MB solution (V_{total} = 30 ml) for 1 h with constant stirring at 250 rpm to establish the equilibrium of dye adsorption/desorption. Subsequently, 10 mg of the sample was immersed in the MB solution (V_{total} = 30 ml) and irradiated with an LED lamp (UV lamp; λ = 365 nm). The reaction mixture (total volume 30.0 ml) was handled in two stages after irradiation. During the first stage, the entire 30 ml suspension was centrifuged in a high-speed centrifuge (Fisherbrand HSE09225, fixed-angle rotor MLA-50) at 25 000 rpm for 5 minutes at 23 °C. Then the second stage was used for kinetic monitoring at each sampling time. 2 ml aliquot was removed from the reaction mixture for centrifugation in a mini centrifuge (Orto Alresa) at 11 500 rpm for 3 minutes; the resulting supernatant was periodically measured (6 steps × 10 min followed by 2 steps × 30 min) by a UV-VIS spectrophotometer (S-200, Boeco) at a wavelength of 670 nm to monitor the degradation rates. After each measurement period, the measured solution was put back into the base solution, and the photocatalytic experiment was carried out further.

Characterization techniques

The surface morphology of CFs and CFs@TiO_2 was studied using a field emission scanning electron microscope (SEM, FEI, Verios 460 L) with an acceleration voltage of 5 kV. The average TiO_2 thickness was calculated using proprietary software, Nanomeasure, from the cross-sectional SEM images. A minimum of 25 measurements were taken using three or four SEM images for each sample. Titanium content in the CFs@TiO_2 samples was detected with an Energy Dispersive X-ray Fluorescence (EDXRF) spectrometer (Elva X PRO, Elvatech, Ukraine). Energy-dispersive X-ray fluorescence spectrometry (EDXRF) was performed using an Elva X Pro spectrometer (Elvatech, Ukraine) to determine Ti content in the samples. The experimental conditions were as follows: X-ray tube voltage of 45 kV, tube current of 266.7 μA, excitation beam filters comprising 300 μm nickel and 300 μm aluminum, a 6.5 mm diameter collimator, spectrum acquisition time of 30 seconds, and measurements conducted under ambient air atmosphere. Mass concentration values (w/w, normalized to 100%) for Ti were calculated using the fundamental parameter model Ti E207, which is incorporated within the instrument's default software package. Each sample was measured eight times, and the results obtained were averaged. The elemental composition was analyzed using an Energy-Dispersive X-ray (EDX) technique with a Tescan MIRA3 XMU scanning electron microscope equipped with an energy-dispersive X-ray detector (Oxford Instruments, UK), operating at an acceleration voltage of 20 kV. The samples' structure was assessed utilizing an X-ray diffractometer (XRD; Smart Lab 3 kW from Rigaku, Japan), configured in Bragg–Brentano geometry with Cu-Kα radiation (λ = 0.154 nm) and equipped with the Dtex-Ultra 1D detector. A current of 30 mA and a voltage of 40 kV were utilized to ignite the Cu radiation. The diffraction patterns were recorded from 10° to 90° with a step size of 0.01° and a scanning speed of 4° per min. Diffuse reflectance spectroscopy (DRS) measurements were conducted over a wavelength range of 200–800 nm utilizing a UV-visible-NIR Jasco V-770 spectrometer equipped with a 16 mm diameter Spectralon-coated integrating sphere and a spectral resolution of 1 nm. Each sample was placed in a quartz cuvette, sealed, and positioned in a sample holder. Raman spectroscopy was conducted utilizing a Witec alpha300R spectroscope (WITec, Ulm, Germany). Raman spectra were acquired in continuous scanning mode within the Raman shift range of 100–2000 cm^{-1}, utilizing a laser excitation wavelength of 633 nm. A 100x objective lens was used to focus the laser beam, resulting in a point with a diameter of 1 μm. The measurement signal was reconstructed through five accumulations with a 20-second integration period. X-ray photoelectron spectroscopy (XPS) measurements were performed on (sample-160c) at room temperature under ultra-high vacuum (UHV) conditions using an Axis Supra XPS system (Kratos Analytical, Manchester, United Kingdom). The equipment was equipped with a monochromatic Al-Kα radiation source of 1486.6 eV and a hemispherical analyzer, which enables a high resolution and sensitivity for surface chemical studies. To eliminate charging effects and provide a better electrical contact during the measurement, the sample was attached directly to the sample holder with double-sided copper tape. The sample analysis chamber (SAC) had a base pressure of less than 3.0×10^{-8} torr during the measurements. The XPS survey spectra were obtained in the binding energy range of 0 to 1200 eV using an emission current of 7 mA and a pass energy of 80 eV with a step size of 1 eV. High-resolution spectra of C 1s, N 1s, O 1s, and Ti 2p were obtained using an emission current of 10 mA with a pass energy of 20 eV and a step size of 0.10 eV. All obtained data were charge-corrected to the adventitious carbon (C 1s) peak at 284.8 eV and analyzed with CasaXPS software version 2.3.25PR1.0 (Casa Software Ltd, Teignmouth, Devon, UK).

Results and discussion

Morphological analysis

Fig. 1 depicts low- and high-magnification SEM images of PAN fibers and PAN fibers infiltrated with TiO_2 after 160 VPI cycles (PAN@TiO_2-160c). The PAN fibers display rough surfaces as they contain shallow ridges, which are common in polymer fibers produced by centrifugal spinning. They are sensitive to the electron beam; thus, their visualization in the SEM is challenging. The PAN@TiO_2-160c shows that the fibers are completely covered with TiO_2 coating. The coating is continuous with a considerably rough surface.

The average diameters of the PAN and PAN@TiO_2-160c fibers (based on statistical analyses) are 0.821 ± 0.07 μm and 0.874 ± 0.07 μm, respectively. The TiO_2 layer wrapping the PAN fiber is indicated in the high magnification figure of PAN@TiO_2 by guiding lines. Based on the thickness assessment from SEM images, the thickness of the TiO_2 layer in the PAN@TiO_2-160c sample was 37.4 ± 7.5 nm. This is significantly thicker than the nominal growth rate of TiO_2 during ALD processes, where typically values around 0.055 nm per ALD cycle were reported.[92] In the present case, given the con-

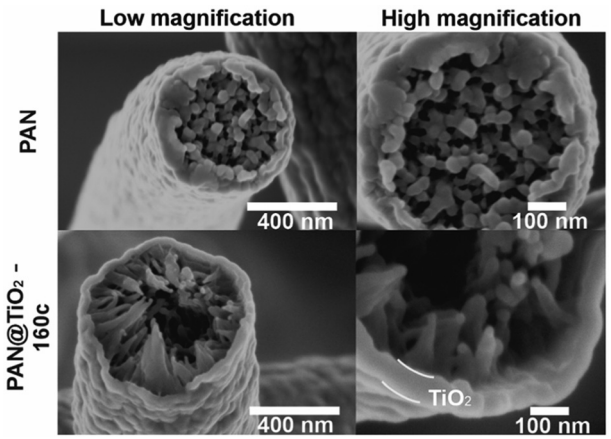

Fig. 1 Cross-sectional SEM images of PAN and PAN@TiO_2-160c fibers at low and high magnification before carbonization.

ditions used, the VPI governs the deposition reactions that occur beneath the surface, resulting in the formation of an organic–inorganic region[93] that makes the whole deposit significantly thicker than the theoretical thickness would be in the corresponding ALD case (*i.e.*, 0.055 nm c^{-1} × 160 cycles = 8.8 nm).

The mechanism of the infiltration[70,93] of TiO_2 by VPI is based on dissolution, diffusion, and reaction of $TiCl_4$ and H_2O with functional groups in PAN. In the first half-cycle, upon exposure of PAN to $TiCl_4$, the precursor dissolves in the polymer and diffuses into the subsurface, with the diffusion depth being a function of various parameters such as temperature, exposure time, polymer density, *etc*. Inside the polymer, $TiCl_4$ will react with functional groups of PAN such as –C≡N or –C═O, or –OH. This results in $TiCl_x$ being chemically bound to the polymer backbone and liberation of volatile HCl as a by-product, which is purged away. In the second half-cycle, the reactive $TiCl_x$-PAN is exposed to H_2O vapor, which hydrolyzes the Ti–Cl bonds forming Ti–$(OH)_x$, and after condensation, TiO_2 nuclei, which gradually coalesce into a nanocrystalline layer with the increasing number of VPI cycles. This infiltration mechanism led to the formation of Ti–N linkages within the hybrid structure, as seen from XPS (to be discussed later). Another practical sign of VPI rather than the ALD process is that the coatings do not readily delaminate from the broken fibers, which would likely occur in the case of sole ALD.

Fig. 2 shows SEM images of CFs@TiO_2 obtained after VPI of PAN fibers with different cycles and subsequent carbonization. Note that the number of VPI cycles has a significant impact on the amount of TiO_2 deposited on/in the CFs. For samples 5c and 10c, the surface appears smooth with no evident TiO_2 coating, suggesting that the deposition is in the initial nucleation phase, in agreement with the literature.[94–97] Sample 20c displays a uniform TiO_2 layer coating with a fine-grained texture. The tiny crystallites spread uniformly and merge to form a continuous oxide, which indicates the initial stages of TiO_2 crystallization. After 40c, a significant change in morphology is observed. The surface becomes considerably rough and further coarsening continues with increased VPI cycles (*i.e.*, 80c and 160c).

Fig. 3 shows cross-sectional SEM images of CFs@TiO_2 for 40c, 80c, and 160c to demonstrate the thickness and uniformity of the nanocrystalline layers. To visualize the TiO_2 layers in more detail, SEM images obtained with a mirror detector are shown in the SI (Fig. S1). For better visibility, the coatings are highlighted by guiding lines. Using statistical analyses of coatings on different spots and on different fibers, the thicknesses of the TiO_2 coatings were estimated to be 15.7 ± 2.4, 22.5 ± 3.7, and 34.7 ± 3.4 nm for 40c, 80c, and 160c, respectively.

The average diameter of the fibers shrunk from 874 ± 7 nm for PAN@TiO_2-160c to 650 ± 19 nm for CFs@TiO_2-160c (based on statistical analyses), which is normal for the carbonization and has been demonstrated in the literature.[90,98–100] However, the thickness of the TiO_2 layer got reduced by 7% after carbonization, measuring 34.7 ± 3.4 nm. This somewhat unexpected outcome can be explained by two factors. Initially, when TiO_2 was deposited on PAN fibers using various VPI cycles (40c, 80c, and 160c), no TiO_2 diffraction peaks were detected (Fig. S2). The lack of peaks can be attributed to the amorphous nature of TiO_2 deposited at a lower VPI temperature. Secondly, there is a TiO_2 surface coating and an infiltrated subsurface, which

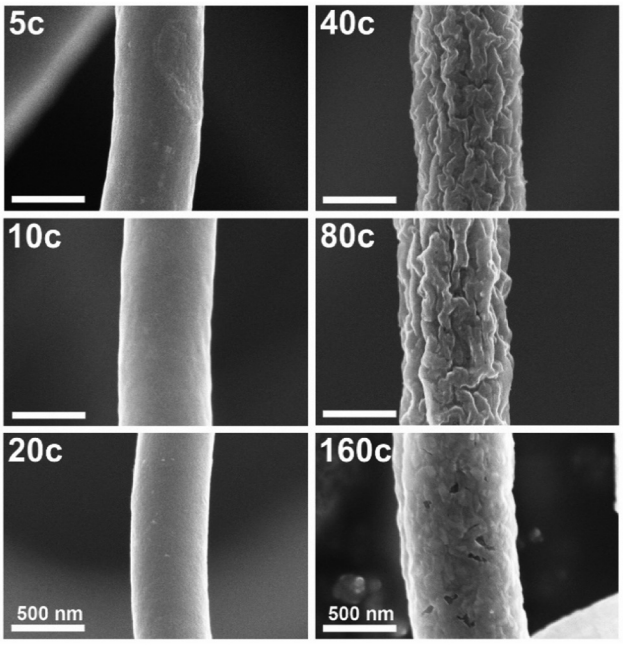

Fig. 2 SEM images of CFs@TiO_2 obtained after TiO_2 VPI of PAN using various cycles and carbonization.

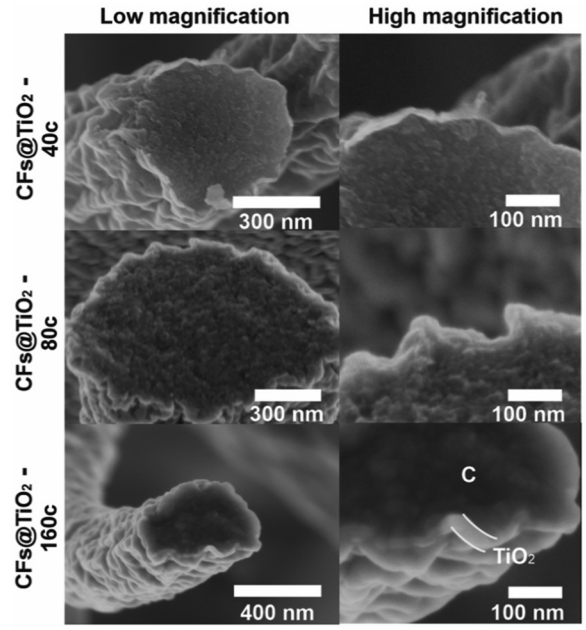

Fig. 3 Cross-sectional SEM images of CFs@TiO_2 fibers (prepared using 40c, 80c and 160c VPI cycles of TiO_2 into PAN and after carbonization) demonstrating the presence and thicknesses of TiO_2 nanocrystalline coatings.

is a hybrid Ti-polymer with a low density extending into the polymer bulk. Upon carbonization at 900 °C, the polymer is decomposed, and infiltrated TiO_2 migrates to the surface to recrystallize with the surface TiO_2. The transformation of the hybrid layer to a purely inorganic will go hand in hand with a compacting of the TiO_2 (through removal of the interstitial organic phase).

Compositional analyses

Energy dispersive X-ray fluorescence (EDXRF and Energy Dispersive X-ray (EDX)) analyses were used to assess the Ti content in CFs@TiO_2 samples that were prepared through various VPI cycles from 5c to 160c. Five independent measurements for each sample were used to achieve statistically rich results. The resulting Ti content (wt%) in CFs@TiO_2 fibers is outlined in Fig. 4. Both techniques revealed a general increase in Ti content with increasing VPI cycles, thus signifying a systematic presence of TiO_2 within the CF. The variability between EDXRF and EDX measurements results from the measuring principles and the characteristic depth of the sampling with each method. EDXRF is sensitive to the bulk, while EDX is more surface-sensitive. The most notable changes were recorded at higher cycles, which is in line with the VPI-driven TiO_2 growth mechanisms. This trend was observed and discussed many times in the literature.[70,71,101] The low standard deviation measured with the samples demonstrates the reproducibility of the measurements based on the samples and the uniformity of the TiO_2 coatings deposited on CFs *via* VPI.

In addition, XPS was performed on sample 160c, which was incorporated in the SI (Fig. S3 and S4). Even though XPS – a highly surface-sensitive technique – is not entirely suitable for this highly porous type of sample, it demonstrates the presence of TiO_2 as the dominant surface species. Additionally, XPS analysis confirms the presence of Ti–N, indicating that nitrogen was also added to the TiO_2 lattice. The analysis showed substitutional β-N (around 396–397 eV) and interstitial γ-N (around 399–401 eV) states, which act as dopants to extend light absorption of TiO_2 into the visible region.

Crystallinity analysis

Fig. 5 demonstrates the XRD patterns of CFs and CFs@TiO_2. Two broad signals for the CFs at roughly 26° and 44.5° are visible, corresponding to graphite (002) and (101) planes, respectively.[102] Samples with low VPI cycles, that is, 5c–20c, do not exhibit a typical TiO_2 diffraction signal, indicating that either the layers are too thin to be detected by X-rays or that the TiO_2 is amorphous. The peak at 44.5°, corresponding to the (101) plane of carbon, typical of hexagonal graphite structures, is observed in all samples. This shows that the core CF structure is not affected even after depositing TiO_2 with various VPI cycles. For sample 160c, diffraction peaks of anatase TiO_2 [JCPDS # 75-1537] evolve at 25.7°, 38.4°, 48.9°, 55.5°, 64°, 69.9°, and 76.8°, matching the (101), (004), (200), (211), (204) and (215) crystal faces, respectively. Note that the intensity of the TiO_2 diffraction peaks increased with increasing VPI cycle number. From the (101) anatase peak, the crystallite sizes in these samples were determined using Scherrer's equation.[103] The crystallite sizes were determined to be 3 nm for the 40c, 3.17 nm for the 80c, and 5.26 nm for the 160c, respectively, which could have an impact on photocatalytic degradation.

Raman analysis

The XRD patterns of CFs@TiO_2 show that the main anatase peak at 25.7° (101) is not well visible, because of the broad amorphous signal from the CFs that masks it. To obtain more information on the structure and composition of CFs@TiO_2, Raman spectroscopy (RS) was employed as it is highly surface-sensitive and can provide more details about the surface species.

Fig. 6 shows Raman spectra of blank CFs and the various CFs@TiO_2. No Raman signals associated with TiO_2 were observed for the 5c, 10c, and 20c samples. Therefore, these

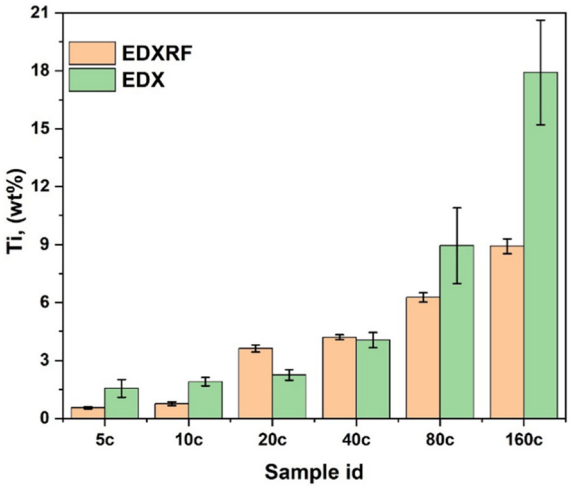

Fig. 4 Comparison of the Ti content (wt%) in CFs@TiO_2 fibers analysed by EDXRF and EDX.

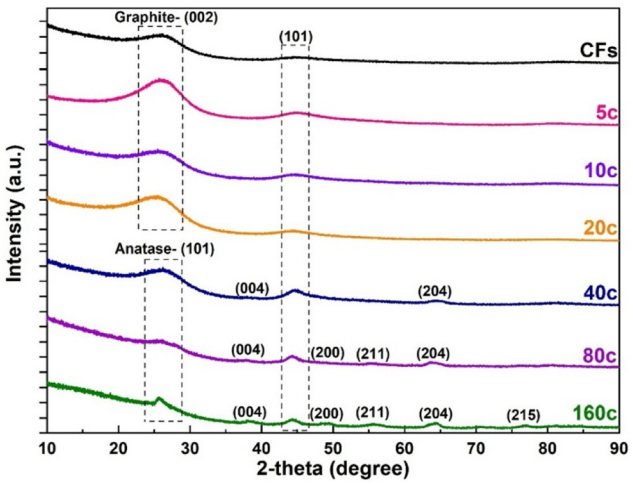

Fig. 5 XRD patterns of CFs and CFs@TiO_2 obtained after VPI processing of CF using various VPI TiO_2 cycles.

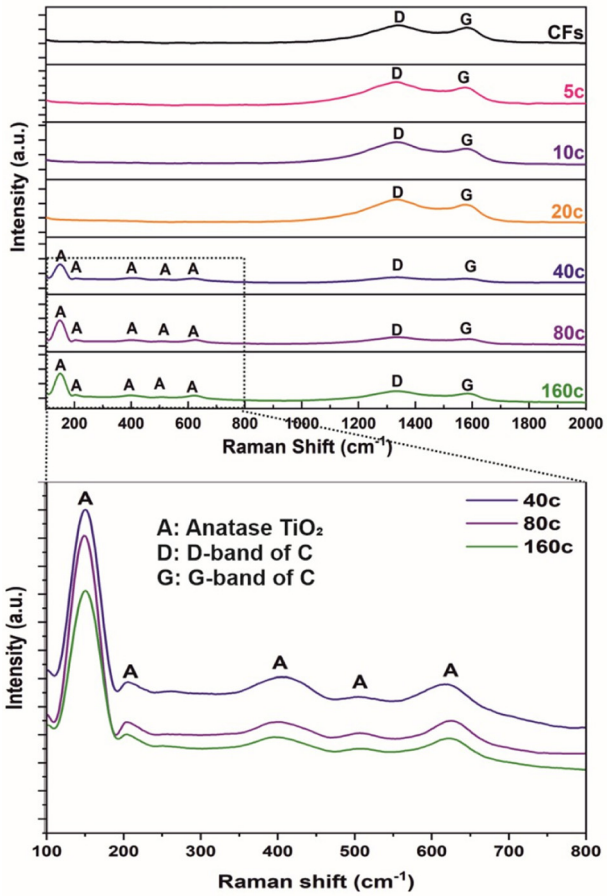

Fig. 6 Raman spectra of CFs and CFs@TiO_2 obtained after VPI processing of CF with various VPI TiO_2 cycles.

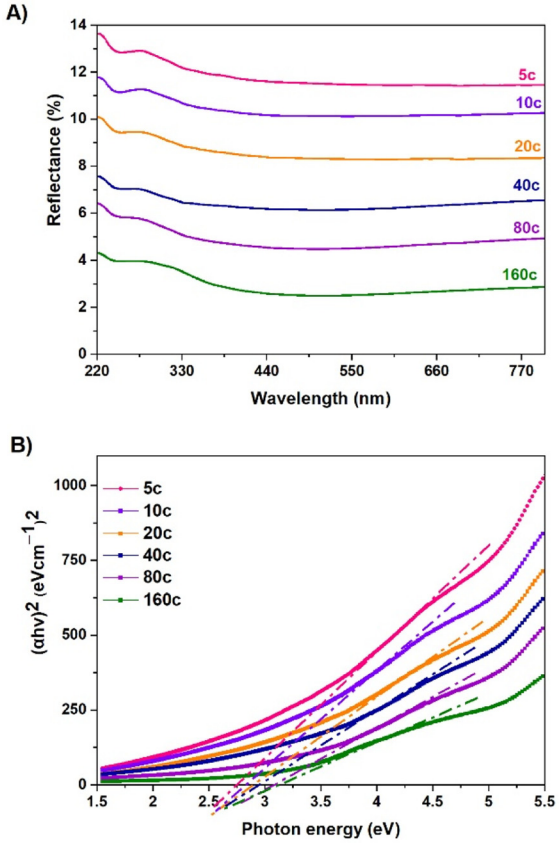

Fig. 7 (A) UV-Vis diffuse reflectance spectra (DRS) of CFs@TiO_2 with various VPI TiO_2 cycles and (B) Kubelka–Munk curves for an estimation of the optical band gap for CFs@TiO_2.

samples are very likely amorphous or, due to their ultralow thickness, have too low amounts of TiO_2 to be detected. As the VPI cycles increased from 40c to 160c, Raman characteristic peaks of the TiO_2 anatase phase began to appear, as can be seen in the magnified spectral sections. Five Raman active modes of anatase TiO_2 were observed at 150, 204, 395, 508, and 622 cm^{-1}, respectively, with symmetries $E_{g(1)}$, $E_{g(2)}$, B_{1g}, A_{1g}, and $E_{g(3)}$[104] in all samples. The spectra further show two bands, one at 1580 cm^{-1} (G band) for a graphitic structure with sp^2 hybridization, and another around 1330 cm^{-1} (D band) for defects in the hexagonal graphitic structure.[105,106] The I_D/I_G intensity ratio was 1.39, 1.37, to 1.27 for 40c, 80c, and 160c. The decrease in I_D/I_G from 1.39 to 1.27 indicates improved graphitic order in the CFs. Lower I_D/I_G values correspond to fewer defect-related trap sites, enabling more efficient electron transport and reduced recombination.[33,107] This supports the higher photocatalytic rate observed for the 160c sample.

UV-Vis analysis

CFs@TiO_2 were further characterized using UV-Vis diffuse reflectance spectroscopy (DRS). From Fig. 7A, the reflectance spectra of CFs@TiO_2 revealed a redshift (to longer wavelengths), thereby extending the absorption range from UV (220–400 nm) to visible (400–800 nm).

The optical band gap energies in Fig. 7B were calculated by applying the Kubelka–Munk theory[108] to the Tauc plot of $(\alpha h\nu)^2$ *vs.* $h\nu$, where α is the absorption coefficient, h is Planck's constant, and ν is the radiation frequency. The optical bandgap energy (E_g) was determined as the point of intersection between the linear parts of the Tauc plot against the abscissa axis and extrapolated. The samples also showed that the calculated band gap energies increased with the VPI cycles: 2.74 eV (5c), 2.83 eV (10c), 2.89 eV (20c), 2.95 eV (40c), 3.07 eV (80c), and 3.14 eV (160c). The increase in band gap energy from 5c to 160c is attributed to the contributions of structural strain,[109] quantum confinement,[110] the creation of oxygen vacancies[111] and the chemical interaction between TiO_2 and CFs.[112]

Photocatalytic activity

The photocatalytic activity of CFs@TiO_2 was examined for the photodegradation of MB under UV light irradiation (λ = 365 nm). Both oxidation reactions (driven by holes and reactive oxide species) and reduction reactions (driven by electrons) occur concurrently during the photocatalytic degradation of MB. When these reactions occur simultaneously, MB breaks

down into CO_2, water, and other less hazardous compounds.[113]

The apparent reaction rate constants (k_{app}) were obtained using the pseudo-first-order approach based on the Langmuir–Hinshelwood (L–H) mechanism,[114] which is valid under low concentration conditions where KC $\ll$ 1 is satisfied.[115,116] Using this condition, the equation for degradation kinetics is as follows: $-\ln(C/C_0) = k_{app}t$.[117] Thus, k_{app} was obtained from the slope of $\ln(C/C_0)$ *versus* time, which is a commonly used approach for photocatalytic degradation of organic dyes.[114]

Fig. 8 shows a linear relationship between $\ln(C/C_0)$ and time. C_0 (mg L^{-1}) and C (mg L^{-1}) are the initial and residual concentrations of MB, respectively, while t is the reaction time and k_{app} is the apparent reaction rate constant. The photocatalytic findings for CFs and CFs@TiO_2 after various VPI cycles (5c, 10c, 20c, 40c, 80c, and 160c) show MB degradation rates of $k = 4.5085 \times 10^{-5}$, 1.893×10^{-4}, 3.71×10^{-4}, 7.601×10^{-4}, 0.00193, 0.00302, and 0.00424 min^{-1}, respectively.

Besides, the linear correlation coefficients (R^2) for CFs@TiO_2 were 0.983, 0.991, 0.992, 0.992, 0.996, and 0.995 for 5c, 10c, 20c, 40c, 80c, and 160c VPI cycles. It was found that the correlation coefficients R^2 values exceeded 0.98 for all CFs@TiO_2 samples, which means the experimental data describe a first-order kinetic equation quite well.

Fig. 9 shows an overall photocatalytic trend based on statistical assessment of two independent measurements (Test 1 and Test 2), with the results presented as mean ± standard deviation. The rate of photocatalytic degradation is mainly determined by the number of reactive species, such as hydroxyl radicals ($^{\bullet}OH$) and superoxide radicals ($^{\bullet}O_2^-$), whose quantity increases with increasing photocatalyst surface[118,119] and is also influenced by an effective charge separation (electrons from holes). In the previous research on TiO_2 nanotubes[120] Scavenging experiments indicated that $^{\bullet}O_2^-$ was the dominant reactive species, which caused MB degradation.

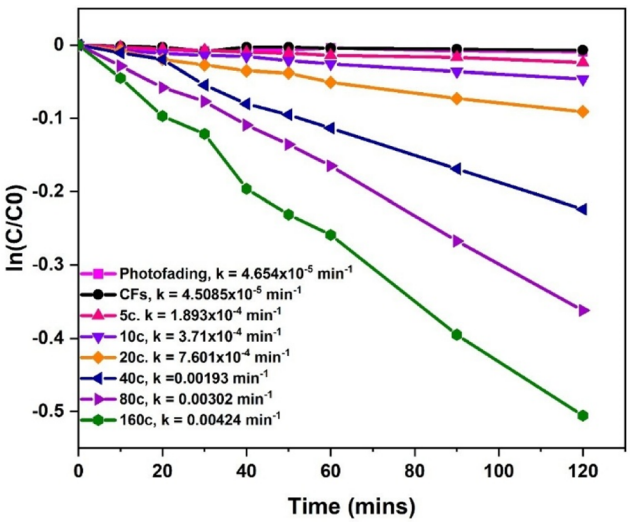

Fig. 8 Photocatalytic degradation kinetics curves of MB for CFs@TiO_2 and the corresponding rate constants.

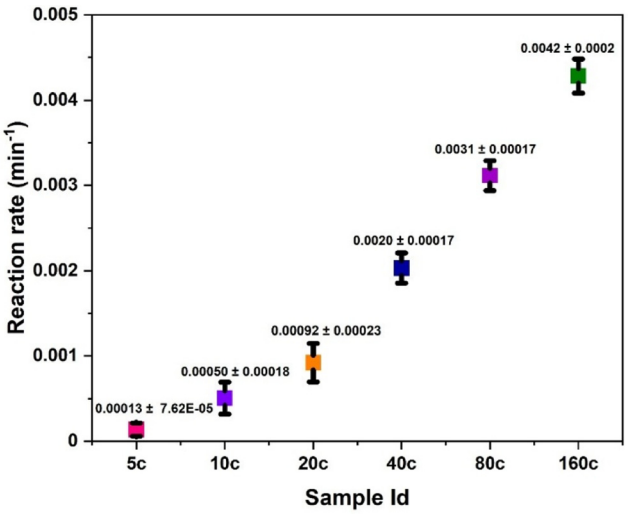

Fig. 9 Variation of MB degradation rates for CFs@TiO_2.

Given that the current system is studied under similar conditions, we expect that the same mechanism will dictate the photocatalytic process.

In addition, according to previous research, thickness,[121] crystallite size,[122] and crystalline structure[123] are important factors influencing photocatalytic activity.[124,125] XRD shows that crystallite size increases from 3 to 5.26 nm with increasing VPI cycles from 40c to 160c, with the 160c sample exhibiting the largest crystallites, SEM inspection of all samples (as shown in Fig. 2 and 3) reveals that the TiO_2 layer produced by 160c is the thickest (34.7 ± 3.39 nm), and also 160c exhibited the highest activity (k = 0.00424 min^{-1}). A moderate increase in crystallite size can lower grain boundaries and suppress electron–hole recombination, thus enhancing photocatalytic performance. In contrast, excessive growth may introduce lattice strain, oxygen vacancies, and other defects that act as recombination centers, as reported in previous studies.[126–128]

In our samples, the enhanced photocatalytic performance is primarily attributed to the increased TiO_2 thickness and the corresponding higher number of active sites. Recombination effects would only become predominant at much higher thicknesses, which we deliberately avoided. However, we wanted to study thinner TiO_2 coatings, which do not clog the fibers and spaces in between. Significantly denser coatings would have a negative impact on fiber morphology, light absorption, *etc*.

The results are in agreement with studies that demonstrate a direct relation, within the nanoscale, between a larger crystallite size and higher photocatalytic activity.[129,130] The optimal band gap is also a critical factor in the photocatalytic performance of a material. The 160c sample in this study had an optical bandgap of 3.14 eV, which is slightly lower than the typical value of 3.2 eV for anatase TiO_2.[131] This may be attributed to the additive contribution of Ti–N doping and the more effective separation of charge carriers, which promotes the absorption of visible light and, as a result, increases the rates of photocatalytic degradation.

Photocatalytic repeatability

To demonstrate an excellent stability of CFs@TiO_2 and the corresponding stability of the photocatalytic performance, the three best-performing samples-40c, 80c, and 160c – were tested in two additional MB decomposition experiments. Overall, photocatalytic experiments for these 3 samples were conducted 4 times in total. Results are shown as Test 3 (Fig. S5) and Test 4 (Fig. S6). The degradation rates in test 3 for 40c, 80c, and 160c are 0.00181 cm^{-1}, 0.00292 cm^{-1}, and 0.00443 cm^{-1}, respectively. The degradation rates in test 4 for 40c, 80c, and 160c are 0.00214, 0.00313, and 0.00403 min^{-1}, respectively. These findings indicate a high degree of consistency between the two independent experiments, with only minimal rate variations ranging from 0.00021 min^{-1} to 0.0004 min^{-1}. In addition, the overall trends are evident, and their consistency indicates that these samples exhibit steady photocatalytic efficiency.

Post-catalytic analysis

EDX analyses were performed after the photocatalytic degradation tests to assess if there are any changes in the elemental composition, particularly Ti, O, and C content, for the three best-performing samples, 40c, 80c, and 160c. (Table 1)

After performing the photocatalysis twice, the Ti content in all samples slightly decreased, which is not surprising, as this is the thickest layer used, and some minor amount of TiO_2 may be detached upon mechanical treatment like stirring, fiber separation, *etc.*, which are required for photocatalytic measurements.

Conclusions

In this study, polyacrylonitrile (PAN) fibers, generated by centrifugal spinning, were infiltrated with TiO_2 by VPI using various cycles between 5 and 160 and carbonized to obtain CFs@TiO_2. Morphological, structural, and compositional analyses (SEM, EDX, EDXRF, XRD, Raman, UV–Vis DRS) confirmed a success in forming a uniform, well-adhered, and crystalline TiO_2 layer on CFs. The TiO_2 thickness increased from 15.7 ± 2.4 to 34.7 ± 3.4 nm with an increment of the VPI cycles from 40 to 160, while the Ti amount increased with increasing VPI cycle number, indicating efficient infiltration of the precursor that remained stable upon carbonization. XRD data demonstrated that the crystallite size increased from 3.17 to 5.26 nm with increasing VPI cycles from 40 to 160. Raman spectra confirmed anatase-type TiO_2 with characteristic peaks. UV–Vis data indicated bandgap increases from 2.74 to 3.14 eV with increased cycle number. The photocatalytic results demonstrated that the 160c sample achieved the highest activity (k = 0.00424 min^{-1}), which arises from an optimal interplay of crystallite size and TiO_2 coating thickness. Moreover, the 160c demonstrated very good performance and stability during cycling and post-catalytic tests, indicating the durability of the synthesis approach. These results further demonstrated that a combination of centrifugal spinning, VPI, and carbonization is a scalable route to produce nanostructured carbon–TiO_2 photocatalysts.

Table 1 Post-catalytic EDX Analysis of CFs@TiO_2 of the 3 best samples

	Mass content (wt%)		
Sample ID	Ti	O	C
40c	3.31 ± 0.27	8.23 ± 0.42	88.44 ± 0.22
80c	8.53 ± 0.77	11.95 ± 0.98	79.51 ± 0.87
160c	17.77 ± 2.60	15.22 ± 0.70	67.00 ± 2.32

Author contributions

P. K. C.: writing the original draft of the manuscript, synthesis of CFs@TiO_2, carbonization of CFs, and photocatalytic measurements. M. R.: trial runs of synthesis of CFs@TiO_2, and EDX measurements. S. A.: synthesis of CFs@TiO_2 M. S.: trial runs on photocatalytic measurements. M. K.: carbonization, reviewing, and editing. M. P.: EDXRF measurements V. C.: production of PAN fibers by centrifugal spinning. K. M.: reviewing and editing. M. K.: writing – reviewing and editing, resources J. M. M.: supervision, conceptualization, writing – reviewing and editing, resources.

Conflicts of interest

The authors declare that the research was conducted without any commercial or financial relationships that could be construed as a potential conflict of interest.

Data availability

The data supporting this article have been included as part of the supplementary information (SI). Supplementary information is available. See DOI: https://doi.org/10.1039/d5nr04109k.

Acknowledgements

Ministry of Education, Youth and Sports of the Czech Republic is gratefully acknowledged for the financial support of the CEMNAT (project LM2023037) and CzechNanoLab (project LM2023051) large research infrastructures, enabling the synthesis of fibers, photocatalytic experiments and EDXRF measurements at CEMNAT and enabling SEM, EDX, XRD, Uv-Vis, and Raman characterization at the CEITEC Nano Large Research Infrastructure. M. K. and S. A. acknowledge funding through PID2022-140861OB-I00 and the Maria de Maeztu Units of Excellence Program grant CEX2020-001038-M funded by MICIU/AEI/10.13039/501100011033 and the European Union through FEDER and "NextGenerationEU"/"PRTR". PKC is grateful to Dr Ivan Saldan for the training on the ultracentrifuge.

References

1 S.-L. Chiam, S.-Y. Pung and F.-Y. Yeoh, *Environ. Sci. Pollut. Res.*, 2020, **27**, 5759–5778.
2 H. Gomaa, M. Y. Emran and M. A. El-Gammal, in *Handbook of Biodegradable Materials*, Springer, 2023, pp. 781–809.
3 X. Zhang, Y. Li, M. Li, H. Zheng, Q. Du, H. Li, Y. Wang, D. Wang, C. Wang, K. Sui, H. Li and Y. Xia, *Int. J. Cloth. Sci. Technol.*, 2020, **32**, 307–321.
4 A. Krishna Moorthy, B. Govindarajan Rathi, S. P. Shukla, K. Kumar and V. Shree Bharti, *Environ. Toxicol. Pharmacol.*, 2021, **82**, 103552.
5 A. Mills, P. Grosshans and D. Hazafy, *Analyst*, 2010, **135**, 33–35.
6 E. Nyankson and R. V. Kumar, *Mater. Today Adv.*, 2019, **4**, 100025.
7 I. Khan, K. Saeed, I. Zekker, B. Zhang, A. H. Hendi, A. Ahmad, S. Ahmad, N. Zada, H. Ahmad and L. A. Shah, *Water*, 2022, **14**, 242.
8 V. K. Jothi, K. Ganesan, A. Natarajan and A. Rajaram, *J. Fluoresc.*, 2021, **31**, 427–436.
9 J. Wang and H. Chen, *Sci. Total Environ.*, 2020, **704**, 135249.
10 M. X. Zhu, L. Lee, H. H. Wang and Z. Wang, *J. Hazard. Mater.*, 2007, **149**, 735–741.
11 S. S. Chan, K. S. Khoo, K. W. Chew, T. C. Ling and P. L. Show, *Bioresour. Technol.*, 2022, **344**, 126159.
12 J. Kim, Y. Chung, D. Shin, M. Kim, Y. Lee, Y. Lim and D. Lee, *Desalination*, 2003, **151**, 1–9.
13 G. Chen, *Sep. Purif. Technol.*, 2004, **38**, 11–41.
14 S. Hube, M. Eskafi, K. F. Hrafnkelsdóttir, B. Bjarnadóttir, M. Á. Bjarnadóttir, S. Axelsdóttir and B. Wu, *Sci. Total Environ.*, 2020, **710**, 136375.
15 M. N. Chong, B. Jin, C. W. K. Chow and C. Saint, *Water Res.*, 2010, **44**, 2997–3027.
16 M. A. Lazar, S. Varghese and S. S. Nair, *Catalysts*, 2012, **2**, 572–601.
17 D. Bahnemann, *Sol. Energy*, 2004, **77**, 445–459.
18 X. Tang, H. Zheng, H. Teng, Y. Sun, J. Guo, W. Xie, Q. Yang and W. Chen, *Desalin. Water Treat.*, 2016, **57**, 1733–1748.
19 U. von Gunten, *Environ. Sci. Technol.*, 2018, **52**, 5062–5075.
20 L. Cermakova, I. Kopecka, M. Pivokonsky, L. Pivokonska and V. Janda, *Sep. Purif. Technol.*, 2017, **173**, 330–338.
21 V. Colla, T. A. Branca, F. Rosito, C. Lucca, B. P. Vivas and V. M. Delmiro, *J. Cleaner Prod.*, 2016, **130**, 103–115.
22 M. Yang, G. Ma, H. Yang, Z. Xiaoqiang, W. Yang and H. Hou, *J. Alloys Compd.*, 2023, **941**, 168995.
23 P. Jain, A. Kumar, N. Verma and R. K. Gupta, *Sol. Energy*, 2019, **189**, 35–44.
24 A. Fujishima, T. N. Rao and D. A. Tryk, *J. Photochem. Photobiol., C*, 2000, **1**, 1–21.
25 K. Rajeshwar, M. E. Osugi, W. Chanmanee, C. R. Chenthamarakshan, M. V. B. Zanoni, P. Kajitvichyanukul and R. Krishnan-Ayer, *J. Photochem. Photobiol., C*, 2008, **9**, 171–192.
26 S. Rehman, R. Ullah, A. M. Butt and N. D. Gohar, *J. Hazard. Mater.*, 2009, **170**, 560–569.
27 S. H. S. Chan, T. Yeong Wu, J. C. Juan and C. Y. Teh, *J. Chem. Technol. Biotechnol.*, 2011, **86**, 1130–1158.
28 J. Schneider, M. Matsuoka, M. Takeuchi, J. Zhang, Y. Horiuchi, M. Anpo and D. W. Bahnemann, *Chem. Rev.*, 2014, **114**, 9919–9986.
29 A. Di Mauro, M. Cantarella, G. Nicotra, V. Privitera and G. Impellizzeri, *Appl. Catal., B*, 2016, **196**, 68–76.
30 S. Zhang, H. Li and Z. Yang, *J. Alloys Compd.*, 2017, **722**, 555–563.
31 H. R. Pouretedal and A. Kadkhodaie, *Chin. J. Catal.*, 2010, **31**, 1328–1334.
32 D. R. Eddy, M. D. Permana, L. K. Sakti, G. A. N. Sheha, Solihudin, S. Hidayat, T. Takei, N. Kumada and I. Rahayu, *Nanomaterials*, 2023, **13**, 704.
33 G. Rajender, J. Kumar and P. K. Giri, *Appl. Catal., B*, 2018, **224**, 960–972.
34 D. O. Scanlon, C. W. Dunnill, J. Buckeridge, S. A. Shevlin, A. J. Logsdail, S. M. Woodley, C. R. A. Catlow, M. J. Powell, R. G. Palgrave and I. P. Parkin, *Nat. Mater.*, 2013, **12**, 798–801.
35 F. Teng, G. Zhang, Y. Wang, C. Gao, L. Chen, P. Zhang, Z. Zhang and E. Xie, *Appl. Surf. Sci.*, 2014, **320**, 703–709.
36 O. Ola and M. Mercedes Maroto-Valer, *J. Catal.*, 2014, **309**, 300–308.
37 B. Lu, X. Li, T. Wang, E. Xie and Z. Xu, *J. Mater. Chem. A*, 2013, **1**, 3900–3906.
38 B. Lu, C. Zhu, Z. Zhang, W. Lan and E. Xie, *J. Mater. Chem.*, 2011, **22**, 1375–1379.
39 R. Sellappan, J. Sun, A. Galeckas, N. Lindvall, A. Yurgens, A. Y. Kuznetsov and D. Chakarov, *Phys. Chem. Chem. Phys.*, 2013, **15**, 15528–15537.
40 Y.-C. Pu, G. Wang, K.-D. Chang, Y. Ling, Y.-K. Lin, B. C. Fitzmorris, C.-M. Liu, X. Lu, Y. Tong and J. Z. Zhang, *Nano Lett.*, 2013, **13**, 3817–3823.
41 A. K. Chandiran, M. K. Nazeeruddin and M. Grätzel, *Adv. Funct. Mater.*, 2014, **24**, 1615–1623.
42 M. Hu, J. Sun, Y. Rong, Y. Yang, L. Liu, X. Li, M. Forsyth, D. R. MacFarlane and H. Han, *J. Power Sources*, 2014, **248**, 283–288.
43 X. Chen, L. Liu, P. Y. Yu and S. S. Mao, *Science*, 2011, **331**, 746–750.
44 L. Liu, P. Y. Yu, X. Chen, S. S. Mao and D. Z. Shen, *Phys. Rev. Lett.*, 2013, **111**, 065505.
45 F. Teng, M. Li, C. Gao, G. Zhang, P. Zhang, Y. Wang, L. Chen and E. Xie, *Appl. Catal., B*, 2014, **148**, 339–343.
46 D. Gu, Y. Lu, B. Yang and Y. Hu, *Chem. Commun.*, 2008, 2453–2455.
47 B. Liu, L.-M. Liu, X.-F. Lang, H.-Y. Wang, X. W. D. Lou and E. S. Aydil, *Energy Environ. Sci.*, 2014, **7**, 2592–2597.
48 L.-W. Zhu, L.-K. Zhou, H.-X. Li, H.-F. Wang and J.-P. Lang, *Mater. Lett.*, 2013, **95**, 13–16.
49 F. Teng, G. Zhang, Y. Wang, C. Gao, L. Chen, P. Zhang, Z. Zhang and E. Xie, *Appl. Surf. Sci.*, 2014, **320**, 703–709.

50 G. Cui, W. Wang, M. Ma, M. Zhang, X. Xia, F. Han, X. Shi, Y. Zhao, Y.-B. Dong and B. Tang, *Chem. Commun.*, 2013, **49**, 6415–6417.
51 P. Kumar Chennam, M. Sepúlveda, M. Rihova, M. Alijani, M. Kachlík, R. Zazpe, D. Pavlinak, K. Maca and J. M. Macak, *Front. Nanotechnol.*, 2024, **6**, 1483917.
52 J. Shi, J. Zheng, P. Wu and X. Ji, *Catal. Commun.*, 2008, **9**, 1846–1850.
53 T. Hashishin, J. Murashita, A. Joyama and Y. Kaneko, *J. Ceram. Soc. Jpn.*, 1998, **106**, 1–5.
54 S. Yao, J. Li and Z. Shi, *Particuology*, 2010, **8**, 272–278.
55 H. Hu, B. Pang, Y. Zhu and Y. Fu, *Text. Res. J.*, 2017, **87**, 2233–2241.
56 S. P. Sharma, C. K. Chang and J.-M. Ting, *Thin Solid Films*, 2014, **570**, 343–350.
57 D. M. Giolando, J. R. Kirchhoff, H. Mueller, P. Q. Nguyen and I. N. Odeh, *Chem. Vap. Deposition*, 2002, **8**, 93–98.
58 S. Galyshev and E. Postnova, *Fibers*, 2021, **9**, 33.
59 O. Sneh, R. B. Clark-Phelps, A. R. Londergan, J. Winkler and T. E. Seidel, *Thin Solid Films*, 2002, **402**, 248–261.
60 V. Pore, A. Rahtu, M. Leskelä, M. Ritala, T. Sajavaara and J. Keinonen, *Chem. Vap. Deposition*, 2004, **10**, 143–148.
61 M. Ritala, M. Leskela and H. S. Nalwa, *Deposition and processing of thin films*, 2002, vol. 1, p. 103.
62 M. Rihova, O. Yurkevich, M. Motola, L. Hromadko, Z. Spotz, R. Zazpe, M. Knez and J. M. Macak, *Nanoscale Adv.*, 2021, **3**, 4589–4596.
63 R. Zazpe, H. Sopha, J. Prikryl, M. Krbal, J. Mistrik, F. Dvorak, L. Hromadko and J. M. Macak, *Nanoscale*, 2018, **10**, 16601–16612.
64 P. Nunez, M. H. Richter, B. D. Piercy, C. W. Roske, M. Cabán-Acevedo, M. D. Losego, S. J. Konezny, D. J. Fermin, S. Hu and B. S. Brunschwig, *J. Phys. Chem. C*, 2019, **123**, 20116–20129.
65 F. Dvorak, R. Zazpe, M. Krbal, H. Sopha, J. Prikryl, S. Ng, L. Hromadko, F. Bures and J. M. Macak, *Appl. Mater. Today*, 2019, **14**, 1–20.
66 G. N. Parsons, S. M. George and M. Knez, *MRS Bull.*, 2011, **36**, 865–871.
67 G.-M. Kim, S.-M. Lee, G. H. Michler, H. Roggendorf, U. Gösele and M. Knez, *Chem. Mater.*, 2008, **20**, 3085–3091.
68 G. K. Hyde, K. J. Park, S. M. Stewart, J. P. Hinestroza and G. N. Parsons, *Langmuir*, 2007, **23**, 9844–9849.
69 G.-M. Kim, S.-M. Lee, G. H. Michler, H. Roggendorf, U. Gösele and M. Knez, *Chem. Mater.*, 2008, **20**, 3085–3091.
70 I. Azpitarte and M. Knez, *MRS Commun.*, 2018, **8**, 727–741.
71 S.-M. Lee, E. Pippel, O. Moutanabbir, I. Gunkel, T. Thurn-Albrecht and M. Knez, *ACS Appl. Mater. Interfaces*, 2010, **2**, 2436–2441.
72 C. Z. Leng and M. D. Losego, *Mater. Horiz.*, 2017, **4**, 747–771.
73 E. K. McGuinness, F. Zhang, Y. Ma, R. P. Lively and M. D. Losego, *Chem. Mater.*, 2019, **31**, 5509–5518.
74 S. Megelski, J. S. Stephens, D. B. Chase and J. F. Rabolt, *Macromolecules*, 2002, **35**, 8456–8466.
75 T. Subbiah, G. S. Bhat, R. W. Tock, S. Parameswaran and S. S. Ramkumar, *J. Appl. Polym. Sci.*, 2005, **96**, 557–569.
76 M. Rihova, A. E. Ince, V. Cicmancova, L. Hromadko, K. Castkova, D. Pavlinak, L. Vojtova and J. M. Macak, *J. Appl. Polym. Sci.*, 2021, **138**, e49975.
77 K. Sarkar, C. Gomez, S. Zambrano, M. Ramirez, E. De Hoyos, H. Vasquez and K. Lozano, *Mater. Today*, 2010, **13**, 12–14.
78 M. Rihova, S. Azpeitia, K. Cihalova, J. Michalicka, P. K. Chennam, E. Kolibalova, R. Svoboda, Z. Heger, M. Knez and J. M. Macak, *J. Controlled Release*, 2025, **383**, 113777.
79 B. Vazquez, H. Vasquez and K. Lozano, *Polym. Eng. Sci.*, 2012, **52**, 2260–2265.
80 Z. McEachin and K. Lozano, *J. Appl. Polym. Sci.*, 2012, **126**, 473–479.
81 M. Rihova, K. Cihalova, M. Pouzar, M. Kuthanova, L. Jelinek, L. Hromadko, V. Cicmancova, Z. Heger and J. M. Macak, *Appl. Mater. Today*, 2024, **37**, 102151.
82 L. Hromádko, M. Motola, V. Čičmancová, R. Bulánek and J. M. Macak, *Ceram. Int.*, 2021, **47**, 35361–35365.
83 H.-Y. Liu, Y. Chen, G.-S. Liu, S.-G. Pei, J.-Q. Liu, H. Ji and R.-D. Wang, *Mater. Manuf. Processes*, 2013, **28**, 133–138.
84 L. Hromádko, E. Koudelková, R. Bulánek and J. M. Macak, *ACS Omega*, 2017, **2**, 5052–5059.
85 J. Ayala, D. Ramirez, E. Fletes, H. Morales, J. G. Parsons and M. Alcoutlabi, *Nano-Struct. Nano-Objects*, 2021, **28**, 100790.
86 N. N. Joda, M. F. Edelmannová, D. Pavliňák, V. T. Santana, P. K. Chennam, M. Rihova, K. Kočí and J. M. Macak, *Appl. Surf. Sci.*, 2025, **686**, 162132.
87 Y. Lu, M. Yanilmaz, C. Chen, M. Dirican, Y. Ge, J. Zhu and X. Zhang, *ChemElectroChem*, 2015, **2**, 1947–1956.
88 T. S. Natarajan and P. Bhargava, *Ceram. Int.*, 2018, **44**, 11644–11649.
89 E. Fitzer, W. Frohs and M. Heine, *Carbon*, 1986, **24**, 387–395.
90 P. K. Chennam, M. Kachlík, M. Říhová, V. Čičmancová, K. Maca and J. M. Macak, *J. Mater. Res. Technol.*, 2024, **28**, 2199–2205.
91 V. Lachat, V. Varshney, A. Dhinojwala and M. S. Yeganeh, *Macromolecules*, 2009, **42**, 7103–7107.
92 S. K. Kim, S. Hoffmann-Eifert, M. Reiners and R. Waser, *J. Electrochem. Soc.*, 2010, **158**, D6.
93 C. Z. Leng and M. D. Losego, *Mater. Horiz.*, 2017, **4**, 747–771.
94 Y. Zhang, C. Guerra-Nuñez, I. Utke, J. Michler, M. D. Rossell and R. Erni, *J. Phys. Chem. C*, 2015, **119**, 3379–3387.
95 Y. Zhang, C. Guerra-Nuñez, I. Utke, J. Michler, P. Agrawal, M. D. Rossell and R. Erni, *Chem. Mater.*, 2017, **29**, 2232–2238.
96 P. Buabthong, Z. P. Ifkovits, P. A. Kempler, Y. Chen, P. D. Nunez, B. S. Brunschwig, K. M. Papadantonakis and N. S. Lewis, *Energy Environ. Sci.*, 2020, **13**, 4269–4279.
97 M. F. Mazza, M. Cabán-Acevedo, H. J. Fu, M. C. Meier, A. C. Thompson, Z. P. Ifkovits, A. I. Carim and N. S. Lewis, *ACS Mater. Au*, 2022, **2**, 74–78.

98 H. Liu, S. Zhang, J. Yang, M. Ji, J. Yu, M. Wang, X. Chai, B. Yang, C. Zhu and J. Xu, *Polymers*, 2019, **11**, 1150.
99 P. Gutmann, J. Moosburger-Will, S. Kurt, Y. Xu and S. Horn, *Polym. Degrad. Stab.*, 2019, **163**, 174–184.
100 M. S. A. Rahaman, A. F. Ismail and A. Mustafa, *Polym. Degrad. Stab.*, 2007, **92**, 1421–1432.
101 M. Rihova, S. Azpeitia, K. Cihalova, J. Michalicka, P. K. Chennam, E. Kolibalova, R. Svoboda, Z. Heger, M. Knez and J. M. Macak, *J. Controlled Release*, 2025, **383**, 113777.
102 L. Cao, X. Zhou, Z. Li, K. Su and B. Cheng, *J. Power Sources*, 2019, **413**, 376–383.
103 J. Il Langford and A. J. C. Wilson, *J. Appl. Crystallogr.*, 1978, **11**, 102–113.
104 K. Yanagisawa and J. Ovenstone, *J. Phys. Chem. B*, 1999, **103**, 7781–7787.
105 A. Cuesta, P. Dhamelincourt, J. Laureyns, A. Martínez-Alonso and J. M. D. Tascón, *Carbon*, 1994, **32**, 1523–1532.
106 H. Liu, W. Li, D. Shen, D. Zhao and G. Wang, *J. Am. Chem. Soc.*, 2015, **137**, 13161–13166.
107 J. Guo, Y. Zhai, T. Xing, B. Zhu, J. Yang and Y. Gu, *J. Phys. D: Appl. Phys.*, 2025, **58**, 415101.
108 Ł. Haryński, A. Olejnik, K. Grochowska and K. Siuzdak, *Opt. Mater.*, 2022, **127**, 112205.
109 A. Janotti and C. G. Van de Walle, *Rep. Prog. Phys.*, 2009, **72**, 126501.
110 K. M. S. Katubi, A. Jabeen, Z. A. Alrowaili, I. Shakir, M. S. Al-Buriahi and M. F. Warsi, *Desalin. Water Treat.*, 2025, **322**, 101115.
111 R. Dangi, B. Basnet, M. Pandey, S. Bhusal, B. Budhathoki, K. Parajuli, S. K. Tiwari and B. P. Kafle, *Energies*, 2023, **16**, 2653.
112 B. A. El-Sayed, W. A. A. Mohamed, H. R. Galal, H. M. Abd El-Bary and M. A. M. Ahmed, *Egypt. J. Pet.*, 2019, **28**, 247–252.
113 K. Rajeshwar, M. E. Osugi, W. Chanmanee, C. R. Chenthamarakshan, M. V. B. Zanoni, P. Kajitvichyanukul and R. Krishnan-Ayer, *J. Photochem. Photobiol., C*, 2008, **9**, 171–192.
114 H. D. Tran, D. Q. Nguyen, P. T. Do and U. N. P. Tran, *RSC Adv.*, 2023, **13**, 16915–16925.
115 K. V. Kumar, K. Porkodi and F. Rocha, *Catal. Commun.*, 2008, **9**, 82–84.
116 R. W. Matthews, *J. Catal.*, 1988, **111**, 264–272.
117 J. Yu, G. Wang, B. Cheng and M. Zhou, *Appl. Catal., B*, 2007, **69**, 171–180.
118 M. A. Henderson, *Surf. Sci. Rep.*, 2011, **66**, 185–297.
119 U. I. Gaya and A. H. Abdullah, *J. Photochem. Photobiol., C*, 2008, **9**, 1–12.
120 M. Sepúlveda, I. Saldan, A. Mahnaz, V. Cicmancova, J. Michalicka, L. Hromadko, R. Bulánek, H. Sopha and J. M. Macak, *Ceram. Int.*, 2023, **49**, 6764–6771.
121 H. Tada and M. Tanaka, *Langmuir*, 1997, **13**, 360–364.
122 N. S. Allen, N. Mahdjoub, V. Vishnyakov, P. J. Kelly and R. J. Kriek, *Polym. Degrad. Stab.*, 2018, **150**, 31–36.
123 S. J. Tsai and S. Cheng, *Catal. Today*, 1997, **33**, 227–237.
124 G. Kenanakis, D. Vernardou, A. Dalamagkas and N. Katsarakis, *Catal. Today*, 2015, **240**, 146–152.
125 N. Quici, M. L. Vera, H. Choi, G. L. Puma, D. D. Dionysiou, M. I. Litter and H. Destaillats, *Appl. Catal., B*, 2010, **95**, 312–319.
126 W. Kongsuebchart, P. Praserthdam, J. Panpranot, A. Sirisuk, P. Supphasrirongjaroen and C. Satayaprasert, *J. Cryst. Growth*, 2006, **297**, 234–238.
127 D. Wrana, T. Gensch, B. R. Jany, K. Cieślik, C. Rodenbücher, G. Cempura, A. Kruk and F. Krok, *Appl. Surf. Sci.*, 2021, **569**, 150909.
128 M. Strauss, M. Pastorello, F. A. Sigoli, J. M. De Souza E Silva and I. O. Mazali, *Appl. Surf. Sci.*, 2014, **319**, 151–157.
129 K. Tanaka, M. F. V. Capule and T. Hisanaga, *Chem. Phys. Lett.*, 1991, **187**, 73–76.
130 B. Ohtani, Y. Ogawa and S. Nishimoto, *J. Phys. Chem. B*, 1997, **101**, 3746–3752.
131 K. M. Reddy, S. V. Manorama and A. R. Reddy, *Mater. Chem. Phys.*, 2003, **78**, 239–245.

